Mass transport in a highly immiscible alloy on extended shear deformation

Miao Song[a, 1, *], Jia Liu[b], Xiaolong Ma[b], Qin Pang[a], Matthew J. Olszta[b], Joshua Silverstein[b], Madhusudhan R. Pallaka[b], Peter V. Sushko[a], Suveen N. Mathaudhu[b, c, d], Cynthia Powell[b], Arun Devaraj[a], Bharat Gwalani[a, e, *]

[a] Physical and Computational Sciences Directorate, Pacific Northwest National Laboratory, 902 Battelle Boulevard, Richland, WA 99354, USA
[b] Energy and Environmental Directorate, Pacific Northwest National Laboratory, 902 Battelle Boulevard, Richland, WA 99354, USA
[c] Material Science and Engineering Program, University of California, Riverside, CA, 92521, USA
[d] Colorado School of Mines, 1500 Illinois St., Golden, CO 8040, USA
[e] Department of Materials Science and Engineering, North Carolina State University, Raleigh, NC, 27695-7907, USA

Keywords:
Tribology
Immiscible alloys
Nanostructures
Shear deformation
Forced mixing
Atom probe

A B S T R A C T

Forced mixing to a single-phase or supersaturated solid solution (SSS) and its prerequisite microstructure evolution in immiscible systems has been a focus of research for fundamental science and practical applications. Controlling the formation of SSS by shear deformation could enable a material design beyond conventional equilibrium microstructure in immiscible systems. Here, a highly immiscible Cu–50 at.% Cr binary alloy (mixing enthalpy of ~20 kJ mol^{-1}) was employed to investigate the microstructure evolution and localized tendencies of SSS during severe shear deformation. Our results demonstrate the dislocation mediated microstructural refinement process in each phase of the binary alloy and the mechanisms associated with localized solute supersaturation as a function of shear strain. Pronounced grain refinement in the softer Cu phase occurs owing to the strain localization driving the preferential dynamic recrystallization. The grain refinement of the Cr phase, however, is enabled by the progressive evolution of grain lamination, splitting, and fragmentation as a function of shear strain. The solute supersaturation is found to be strongly dependent on the local environments that affect the dislocation activity, including the level of microstructure refinement, the interfacial orientation relationship, the mechanical incompatibility, and the localized preferential phase oxidation. Ab initio simulations confirm that it is more favorable to oxidize Cr than Cu at incoherent Cu/Cr interfaces, limiting the mass transport on an incoherent boundary. Our results unveil the mechanism underpinning the non-equilibrium mass transport in immiscible systems upon severe deformation that can be applied to produce immiscible alloys with superior mechanical properties.

1. Introduction

Solid-phase processing (SPP), including ball milling [1], equal-channel angular extrusion [2], wire drawing [3], high-pressure torsion [4], friction stir processing [5], and shear-assisted processing and extrusion [6], has attracted considerable attention as it can be employed to develop bulk nanostructured materials with desired properties economically. SPP often results in non-equilibrium microstructures with extraordinary physical properties which are otherwise rarely attainable [6]. For example, SPP can produce the supersaturated solid solution (SSS) with refined grain structure along with the hierarchical distribution of nanoscale second phase particles, exhibiting exceptional mechanical properties [7–9]. Nevertheless, due to the dynamical nature of SPP, how the microstructure evolution upon severe deformation affects the mass transport process is still not well understood, especially for immiscible alloys with high mixing enthalpy. Gaining insights into this deformation-mass transport-coupled process down to atomic scale is crucial to predict, control, and optimize the microstructures during SPP, the basis for successful fabrication of high-performance nanostructured alloys.

* Corresponding authors.
E-mail addresses: songmiao@csu.edu.cn (M. Song), bharat.gwalani@pnnl.gov, bgwalan@ncsu.edu (B. Gwalani).
[1] Present address: State Key Laboratory of Powder Metallurgy, Central South University, Changsha 410083, China

To enhance supersaturation and homogenization of microstructures in immiscible alloys, suppress phase separation and precipitation induced by thermally activated diffusion, high deformation rates and low temperatures are often desired during SPP [10]. While simulation studies have reported complete mixing at the atomic scale in immiscible systems even with large positive heat of mixing and substantial lattice mismatch [11], experimental results only observed rather limited solubility extension or mixing in alloy systems such as Cu–Nb [10], Cu–Mo [12], Ag–Fe [13], and Ag–Ni [14], even under high-strain and low-temperature deformation. The underlying mechanisms governing the extent of forced mixing are still a subject of experimental exploration. Generally, the two accepted mechanisms for intermixing and nanoscopic homogenization in immiscible alloys are either mediated by interfaces/grain boundaries [15–17] or by dislocation transfer processes [15, 16]. During SPP, an increase in lattice strain, pile-up of dislocation at the phase interfaces, and refinement of grain can result in a significant increase in interfacial energy, that can serve as the main driving force for non-equilibrium mixing in immiscible alloys [15–18], such as Cu-Ag [16]. The critical crystal size required for non-equilibrium mixing may vary depending on the difference in enthalpies of the constituent elements [19, 20]. Nevertheless, in most of the immiscible alloys with moderate-to-high mixing enthalpies, besides the high interfacial energy accumulated by grain refinement, dislocation transfer from one phase to another plays a key role in forced mixing [15]. One of the important mechanisms for grain refinement assisted chemical mixing induced by dislocation-shuffling and shear banding has been systemically analyzed by Raabe et al. [9] in a Cu-Ag-Nb alloy. There are demanding criteria for this hetero-phase slip transfer to occur, i.e., the resolved shear stress of the dislocations approaching the heterointerface should be a maximum on the activated system, the active slip planes on either side of the interface should be almost parallel, and the configuration at the interface should be one of minimum energy [9, 21]. In addition, it is challenging to keep continuous dislocation transfer across hetero-phase interface during solid-phase processing. The continuous grain refinement and rotation, lattice mismatch, strain accumulation, and localized oxidization can highly influence the crystallographic coherency and mechanical compatibility of the interfaces for dislocation to transfer across. Therefore, understanding the evolution of the local environment of various hetero-phase grains during SPP will facilitate a better understanding of the coupling between deformation and mixing of immiscible alloys.

Binary metal matrix composites with Cu as a matrix have attracted attention because of their remarkable work hardening combined with excellent electrical conductivity [22, 23]. Here, a high mixing enthalpy ($\sim$20 kJ mol^{-1} [24]) Cu–50 at.% Cr binary alloy was employed to reveal the nanoscopic evolution and forced mixing mechanisms of Cu and Cr during severe shear deformation and to explore optimal alloying configurations.

2. Experimental

2.1. Sample preparation and tribological testing

As-cast Cu–50 at.% Cr binary alloy was annealed at 800 °C for 24 h for homogenization. The sample surface was metallographically polished and then shear-deformed using an Anton Paar pin-on-disk tribometer [6]. A 6 mm diameter stainless-steel sphere with a load of 1 N and linear speed of 50 mm/s was used in the reciprocating mode for 1/2 (single pass of tribometer pin) and 10 cycles, with a stroke length of 5 mm and a width of 400 µm (Fig. 1(a)). The directions along with the sliding, normal to the sliding surface, and perpendicular to the sliding direction were defined as SD, ND, and TD, respectively (Fig. 1(b)).

2.2. Plastic strain estimation

Plastic shear strain (PSS, ε) in the Cr phase (Fig. 1(c)) was estimated by observing the shape change of the Cu nanoparticles that are dispersed in the initial Cr grains (Fig. 2(a, b)) observed in the ND–SD sample, i.e., $\varepsilon = D/\sqrt{3}c$ ($D \gg c$) [25], where D is the average diameter of the initial spherical Cu nanoparticles in the Cr grains and c is the average thickness of the sheared Cu nanoparticles. The PSS of the scratch surface was estimated by exponential fitting of the experimental data (Fig. 1(c)). Due to severe shear deformation, the Cu nanoparticles close to the scratch surface ($<$ $\sim$1 µm) cannot be identified clearly. The maximum PSS of the sample under unidirectional wear scratch (1/2 cycle) was estimated by dividing the PSS of the scratch surface after 10 cycles by 20. The shear strain level in the Cu phase was not evaluated due to the lack of microstructural markers inside. To facilitate understanding, the refined Cu grains are termed as Cu nanograins (Cu NGs), whereas the Cu particles in the initial big Cr grains are Cu nanoparticles (Cu NPs), hereafter.

2.3. Microstructure characterization

Scanning electron microscopy (SEM), energy dispersive spectroscopy (EDS), and electron backscatter diffraction (EBSD) were performed using a JEOL JSM-7001F-field emission gun (FEG) SEM instrument with a Bruker xFlash 6060 energy dispersive X-ray spectroscopy and Bruker eFlash high-resolution EBSD (HR-EBSD) detector. A standard focused ion beam (FIB) site-specific lift-out procedure was employed to prepare transmission electron microscopy (TEM) and atom probe tomography (APT) wedge-shaped samples by a gallium (Ga)-based FIB-SEM (Helios NanoLab 600i, Thermo Fisher Scientific, USA) outfitted with an Oxford Instruments Aztec X-Max 80 mm^2 EDS detector operated at 2–30 kV. TEM samples were prepared along ND–SD and ND–TD cross-sections (Fig. 1(b)) and lifted out from the center positions of the scratch width (the white boxed area in Fig. 1(b)). An aberration-corrected environmental transmission electron microscope (ETEM, Thermo Fisher Scientific, USA) was employed at 300 kV for bright-field (BF), selected area electron diffraction (SAED) pattern, and high-resolution TEM (HR-TEM) images. Another aberration-corrected TEM (JEM-ARM200CF from JEOL, Japan) equipped with annular bright-field (ABF) and high-angle annular dark-field (HAADF) detectors, an EDS system, and a precession electron diffraction (PED, NanoMEGAS, UAS) device was employed at 200 kV for ABF-STEM, HAADF-scanning TEM (STEM), composition analysis, inverse pole figure (IPF), and grain boundary (GB) misorientation analysis. The electrons from 8 mrad to 34 mrad and from 68 mrad to 280 mrad were collected for ABF-STEM imaging and HAADF-STEM imaging, respectively. APT analysis was performed using LEAP 4000XHR (CAMECA, USA) under pulsed-laser assisted mode at a pulse laser energy of 20 pJ, a pulsed frequency of 125 kHz, a specimen temperature of 50–60 K, and a detection rate of 0.4% (four evaporation events per 1000 pulses). The average Vickers hardness (92$\pm$7 Hv) of the alloy was measured using 500 g load and 12 s of dwell time. The value was obtained by averaging 20 different locations.

2.4. Ab initio simulation

Vienna Ab initio Simulation Package (VASP) [26,27] was used for all density functional theory (DFT) [28] calculations. The exchange-correlation potential was described using the Perdew–Burke–Ernzerhof (PBE) functional [29,30] with the projector augmented wave potential (PAW) [31]. The plane-wave basis set with 400 eV energy cutoff was used for all calculations. The gamma centered 1 $\times$ 1 $\times$ 1 k-mesh was used for all systems, except for

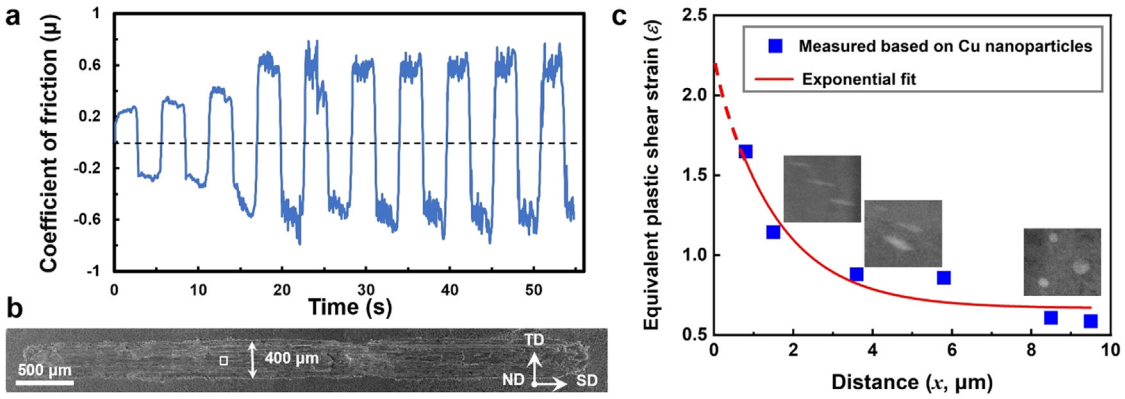

Fig. 1. Tribometer test and calculation of plastic shear strain (PSS). (a) Coefficient of friction (COF)-time curve recorded by the instrument (COF is estimated to be 0.6). (b) Wear track from the top view. The directions along the sliding direction, normal to the sliding surface, and perpendicular to the sliding direction are defined as SD, ND, and TD, respectively. (c) Relationship between the equivalent PSS (ε) and distance from the scratch surface after 10 cycles of shear deformation. Scale bars in (c) are 200 nm.

the KS system, where a 7 × 1 × 1 k-mesh was applied. For all energy minimizations, the convergence criteria were 10^{-5} eV. Bader charge analysis [32] was performed to analyze the charge distribution in selected systems.

3. Results and discussion

3.1. Starting microstructure of Cu–50 at.% Cr

The as-cast Cu–50 at.% Cr binary alloy consists of the Cu matrix (grain size >200 μm, Fig. S1(a) in Supplementary Information) and the Cr dendritic grains (~11.8 ± 6.1 μm size, separated and embedded in the Cu matrix, Figs. 2(a) and S1(a)). In addition to those coarse Cu matrix grains, profuse spherical Cu NPs (average particle size: 54.2 ± 37.4 nm) were also observed in the Cr dendritic grains (Figs. 2(b), S1(c-e), and Movie S1). However, no Cr nanoparticles were detected in the Cu grains. The APT compositional analysis (Fig. 2(c) and (d)) corroborates that the mutual solubility between Cu and Cr is negligible in the starting immiscible Cu-50 at.% Cr alloy (see also the equilibrium phase diagram in Fig. S2). The average composition of Cr dissolved in the Cu matrix is 0.09 at.% ± 0.002 at.%, while the Cu dissolved in the Cr grain is 0.02 at.%± 0.004 at.% based on APT analysis. In addition, to probe the difference in the hardness of the two phases in the binary alloy, we performed micro indentation testing. The average micro indentation hardness of Cr grains (consisting of Cu NPs) is 7.2 ± 1.2 GPa, which is significantly higher than that of Cu grains (2.6 ± 0.2 GPa). This relatively higher hardness of Cu grains, compared with that of the previously reported pure Cu (~1 GPa [33]), is supposed to be associated with the effect of the surrounding Cr/Cu interfaces and/or the Cr grains.

The inverse pole figure (IPF) map (Fig. 3(a) and its inset) suggests that the Cr dendrites in large Cu grains have preferred orientations with respect to their Cu matrix. For example, the inset in Fig. 3(a) shows that $[001]_{Cr}$ dendrites and $[111]_{Cr}$ dendrites are nearly parallel to the surrounding $[101]_{Cu}$ matrix, coinciding with the Nishiyama–Wasserman (N–W) relation ($<001>_{BCC}//<110>_{FCC}$) and the Kurdjumov-Sachs (K-S) relation ($<111>_{BCC}//<110>_{FCC}$), respectively [34–36]. Quantitative analysis of the IPF map shows that N–W and K–S relations (72% combined in Fig. S1(a, b)) dominate the orientation relationship (OR) between the Cu matrix and the inside Cr dendrites. Similarly, the N–W OR (Fig. 3(b, c)) and the K–S OR (Fig. 3(d, e)) are observed between the Cu NPs and the surrounding Cr dendritic grains via HR-TEM and their Fourier transform in the reciprocal space.

Therefore, the three representative microstructure features that were observed in the starting microstructure are (1) dendritic Cr grains, (2) coarse Cu grains, and (3) Cu-rich nanoparticles within Cr dendritic grains. These three features would undergo distinctive microstructure evolution and mass transport between Cr and Cu as a function of the imposed shear strain, which are detailed by site-specific observations in the present study.

3.2. Disparate refinement in Cu and Cr phases under co-deformation

Fig. 4(a–c) shows a typical microstructure obtained after 10 cycles of tribological shear deformation. The PSS values associated with Cr grains are labeled on the left side of Fig. 4(a) at the corresponding depths. The maximum PSS at the scratch surface was estimated to be ~2.3, see also experimental. In the top-most layer (0 ⟨ depth < 2 μm and PSS ⟩ ~1.0 in Cr dendritic grains), Cu NGs and Cr lamellae structures are formed after severe deformation (Figs. 4(a–d) and S3). Moving to the sub-surface layer (depth > 2 μm in Fig. 4(a)), both Cu and Cr phases are primarily composed of equiaxed grains (excluding two Cr lamellae denoted by cyan arrows in Fig. 4(a)) in Cu. Grain size reduction becomes increasingly prominent in Cu and Cr phases when approaching the top surface, i.e., increasing PSS (Fig. 4(d)). Notably, the actual Cr grain size is presumably even larger because only the short dimension of the elongated Cr lamellae is considered in the measurement along ND. It is safe to conclude that the Cu grain size is finer than Cr at the observed depth (< ~8 μm), which is influenced by the tribological shearing, although the starting grain size of Cu (> 200 μm) is larger than that of Cr (11.8 ± 6.1 μm). We observed that the Cu underwent a higher grain refinement than Cr at a similar depth below the scratch (Figs. 4(d) and S4(f)). The soft material (Cu here) can be expected to experience a much larger shear strain due to the preferential strain localization during deformation [37]. The PED results (Fig. 4(e–j)) show that Cu GBs are primarily of high-angle character (lines 1 and 3), suggesting that the grain refinement in Cu is driven by dynamic recrystallization (DRX) [38,39]. In contrast, Cr GBs are dominated by low-angle GBs (lines 2 and 4 in Fig. 4(e–j), see also Fig. 5(e)). Another view of the deformation is provided in Fig. S4, where a TEM sample was lifted out at a 90° rotation (ND–SD direction) compared to that in Fig. 4 (ND-TD direction). The combined observations from both orthogonal directions conclude that most Cu is indeed equiaxed grains (Figs. 4(a), S3, and S4(a–c)). Notably, a few voids were detected at Cu GBs (Fig. S5) and at Cu/Cr interfaces (Fig. S6), similar to observations of other metals during solid-phase deformation [40].

3.3. Recrystallized grains in Cu and Cr

The PED data in Fig. 4(e–j) confirm that the DRX occurred in Cu, especially in the top-most layer, but a pronounced DRX is rarely

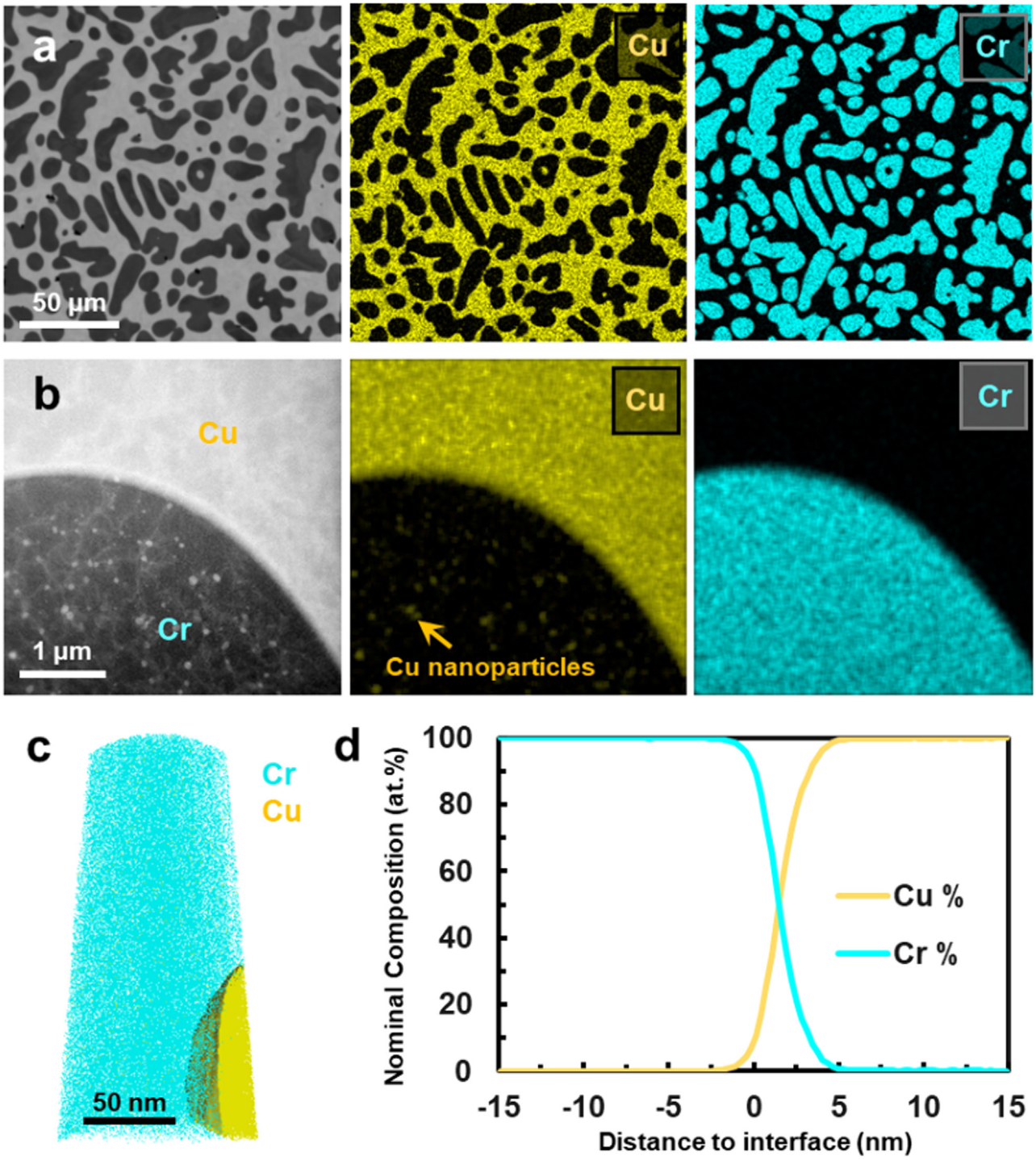

Fig. 2. Microstructure of the Cu–50 at.% Cr binary alloy before deformation. (a) Scanning electron microscopy back scattered electrons (SEM-BSE) image and EDS mapping showing Cr dendritic grains distributed in the Cu matrix. (b) HAADF-STEM image and EDS mapping showing profuse Cu NPs in a Cr grain. (c) 3D atomic map showing the Cu/Cr interface highlighted with 15 at.% Cu isoconcentration surface. (d) Compositional change across the Cu/Cr interface.

seen in Cr phase. As discussed above, this is closely associated with the strain localization in the softer Cu phase [37]. To reveal the difference between Cu and Cr nanograins in the top-most layer, microstructures in nanograins were further analyzed using atomic HAADF-STEM imaging. Extensive twin lamellae in the Cu grain and stacking faults on the top Cu GBs/twin interfaces (highlighted by yellow arrows in Fig. 5(a)) were detected in the top-most layer (~800 nm below the surface). Stacking faults mainly formed near the top GBs/twin interface (Fig. 5(a)) are associated with relatively high shear strain close to the scratch surface. Stacking faults initiating at GBs or twin interfaces facilitate the growth of secondary twin lamellae and the subsequent grain refinement [41,42]. Apart from twin lamellae and stacking faults, almost no perfect dislocation was observed in Cu grains in the top-most layer (Fig. 5(b)), consistent with the PED analysis above (Fig. 4(e–g)), i.e., misorientation angles are negligible inside Cu grains. Nevertheless, profuse edge dislocations were detected in a Cr lamella in the top-most layer (Fig. 5(c, d)), resulting in severe lattice deformation. This is

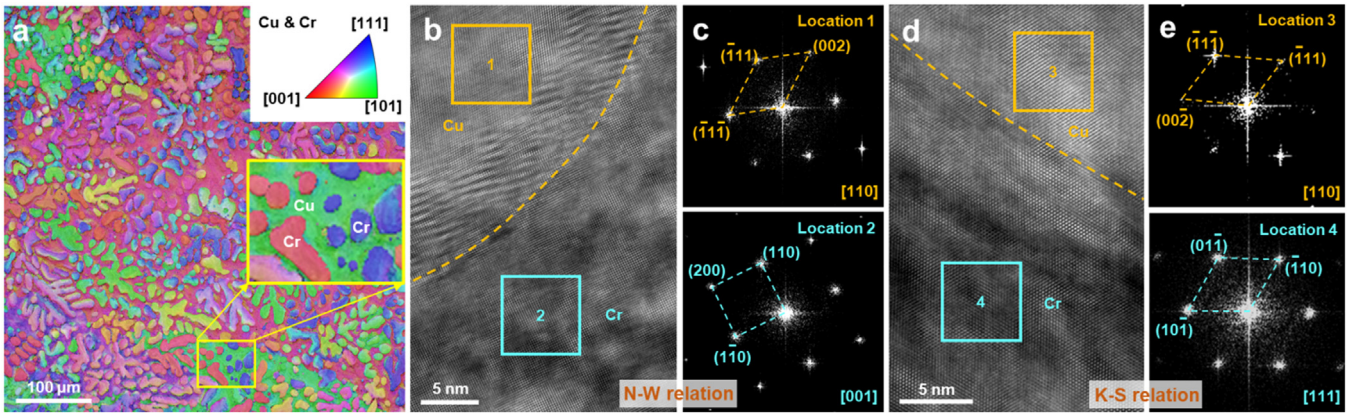

Fig. 3. Orientation relationship between Cu and Cr. (a) Inverse pole figure (IPF) of the Cu–50 at.% Cr binary alloy. Inset comes from the enlarged, yellow-boxed area. (b, d) HR-TEM images of two Cu/Cr interfaces. (c, e) Fast Fourier transform (FFT) images of corresponding locations in (b) and (d), showing N-W and K-S relations, respectively. The Cu/Cr interfaces are roughly outlined by yellow dashed lines. Notably, there is a slight overlap between the Cu particle and the surrounding Cr matrix in (b).

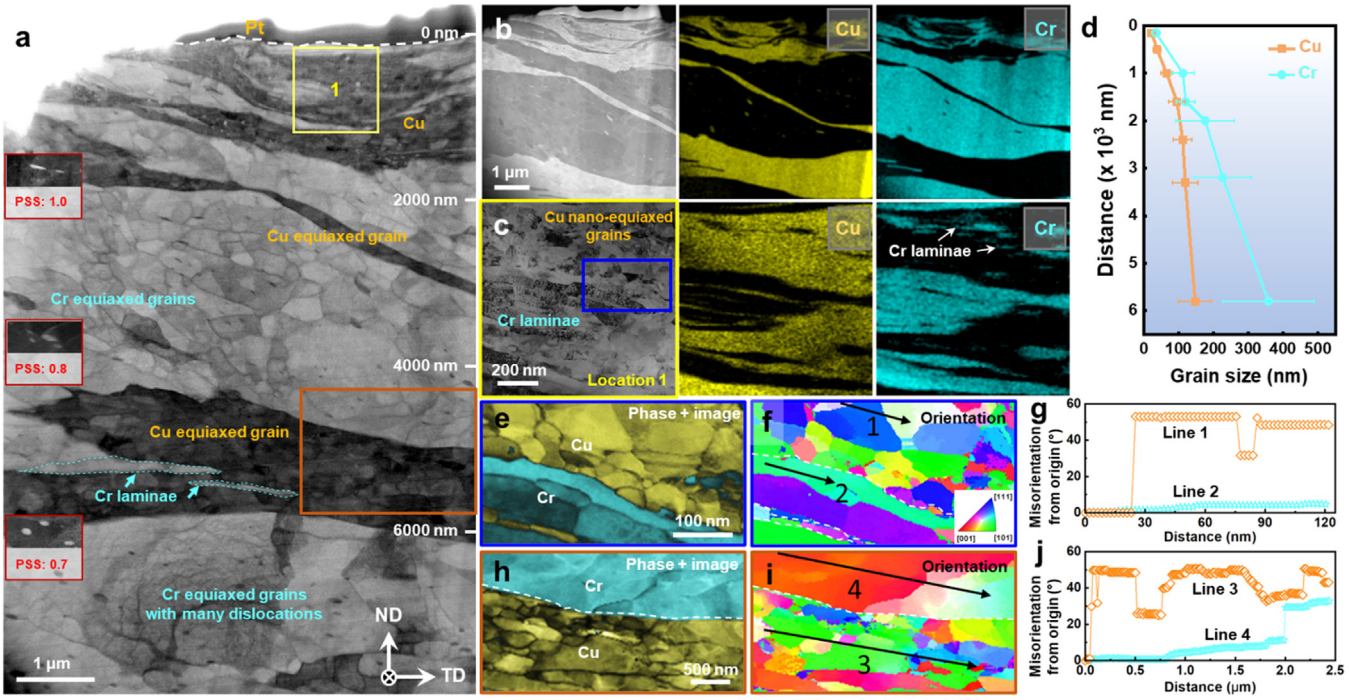

Fig. 4. Microstructures after 10 cycles of severe shear deformation. (a) ABF-STEM image. Inset red boxes show the estimated PSS. (b) HAADF-STEM image and EDS mapping. (c) HAADF-STEM image of the yellow-boxed area in (a) and EDS mapping. (d) Grain sizes evolution of Cu and Cr phases as a function of the distance from the scratch surface. (e, h) Combined images of phases and HAADF-STEM images of the blue-boxed area in (c) and orange-boxed area in (a), respectively, acquired by precession electron diffraction. (f, i) IPFs of areas (e) and (h), respectively. (g, j) Misorientation along lines 1 and 2 in (f) and lines 3 and 4 in (i), respectively.

also verified by dark strain contrast in the Cr lamella (Fig. 5(c)) and misorientation angles inside Cr grains (Fig. 4(e–g)). Besides the formation of Cr lamellae surrounded by Cu in the top-most layer, many low-angle GBs Cr equiaxed grains were detected in the sub-surface (~2.7 μm below, grain size: ~230 nm, Fig. 5(e)), which is also consistent with the observations made by PED in Fig. 4(h–j). In addition, Cr equiaxed grains with profuse dislocations (grain size > ~400 nm, Fig. 4(a)) were also detected at ~6 μm below the scratch surface. Therefore, twins and stacking faults are more favorable modes of deformation in Cu NGs (formed by DRX) in the top-most surface. Nevertheless, grain refinement of Cr lamellae and equiaxed grains is still dominated by dislocation slip in both the top-most layer and the sub-surface, i.e., Cr is still in the early stage of DRX or insignifically observable.

Unidirectional wear scratch (maximum shear strain: ~0.12, Figs. 1(c) and 6) was carried out to further verify the preferential deformation of Cu. The ABF-STEM image (Fig. 6(c)) shows a gradient dislocation density in the Cr grain from the scratch surface (dislocation area density ~6.9 × 10^{13} m^{-2}) to the sub-surface (~2.5 μm below, dislocation density ~4.6 × 10^{12} m^{-2}). This suggests that the influence of deformation depth is ~3.0 μm from the scratch surface in the Cr grains after half-cycle deformation (Fig. 6(a–c)). The microstructure difference between Cu and Cr after half-cycle shear deformation further verifies that deformation in Cu is more pronounced than in Cr. The differences are detailed as follows: (1) Profuse new dislocation cells and/or sub-grains (~1–2 μm, denoted by white arrows in Fig. 6(a)) were detected in the Cu matrix, but relatively fewer dislocations were detected in the Cr grain (Fig. 6(a)). (2) A dislocation pile-up (denoted by the white arrow in Fig. 6(d, e)) and a dislocation cross-slip (denoted by the yellow arrow in Fig. 6(e), see also Movie S1) were detected in the Cu particle (~2.1 μm below), although few disloca-

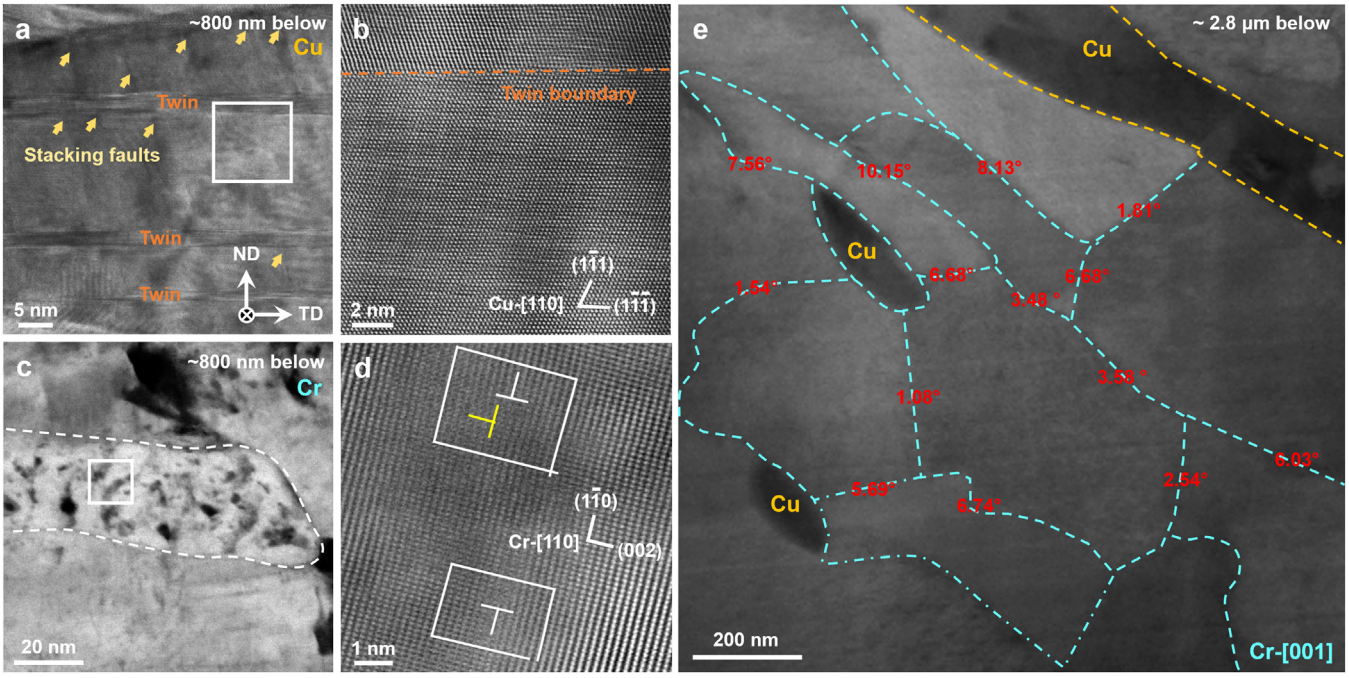

Fig. 5. Defects in Cu and Cr grains in the top-most layers after 10 cycles of severe shear deformation. (a) BF-TEM image showing the formation of twin lamellae and stacking faults in a Cu grain. (b) HAADF-STEM image of the white-boxed area in (a). (c) ABF-STEM image of a Cr lamella (outlined by the white dashed line). (d) HAADF-STEM image of the white-boxed area in (c). Dislocations are denoted by "⊥". (e) BF-TEM image showing many low-angle GBs in Cr and two Cu NPs at Cr GBs. All Cr grains outlined by cyan dashed lines in (e) were aligned close to the [001] zone axis. Misorientation angles between two adjacent Cr grains are labeled on GBs.

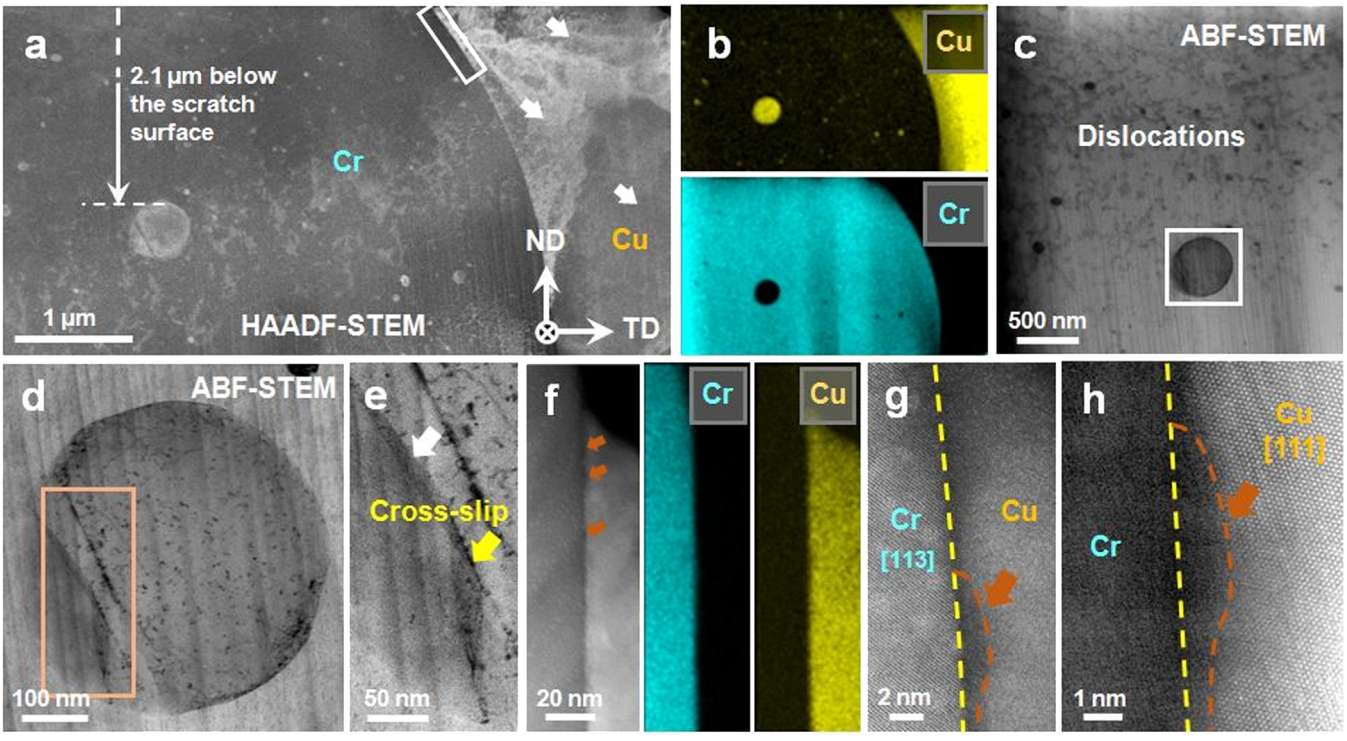

Fig. 6. Microstructure of the Cu/Cr binary alloy after half cycle severe shear deformation. (a) HAADF-STEM image showing the formation of profuse dislocations and sub-grains (denoted by white arrows) in the Cu matrix. (b) EDS mapping. (c) Annular bright-field (ABF) STEM image showing a gradient dislocation density distribution in the Cr grain in (a). (d) ABF-STEM of the enlarged white boxed area in (c). (e) Enlarged yellow-boxed area in (d). (f) HAADF-STEM image and EDS mapping of the enlarged white-box in (a). (g, h) High-magnification HAADF-STEM images showing black contrast areas (denoted by orange arrows) on the side of the Cu grain by tilting the Cr and Cu grains to [113] and [111] zone axes, respectively.

tions were detected in the surrounding Cr grain. (3) Several dark-contrast regions (supposed to be induced by defects/large lattice deformation) were detected on the side of the Cu grain (denoted by orange arrows, Fig. 6(f–h)). Notably, the high-magnification EDS mapping (~0.5 μm below, Fig. 6(f)) verifies that the Cu/Cr interface is straight and Cu/Cr interface migration can be ignored after half-cycle deformation. All these results suggest that there is strain localization in the Cu grains and the Cr/Cu interface acts as a barrier to prevent dislocation motion from Cu to Cr at low shear strains [9, 37] due to the substantial mechanical incompatibility between Cu and Cr with their initial large grain sizes. This strain localization in the Cu grains presumably drives DRX and the substantial microstructural refinement [6], i.e., dislocation mode dominates the initial deformation of Cu grains.

Therefore, taken as a whole, deformation of Cu is dominated by dislocation mode in the sub-surface (PSS $\langle$ ~1.0, grain size $\rangle$ ~180 nm) and by stacking faults and twinning in the top-most layer (PSS $>$ ~1.0, grain size $<$ ~180 nm). For Cr, deformation is dominated by dislocation mode in all observed regions. Consequently, in the top-most layer, Cu underwent DRX, while the Cr phase did not.

3.4. Lamination, splitting, and fragmentation of Cr grains

After 10 cycles of tribological shear deformation, many Cr nano lamellae formed in the top-most layer (Fig. 4(a–c)). Fig. 7 shows the evolution process of Cr lamella with increasing shear strain. As presented in Fig. 7(a), Cr lamellae (~10 nm × 52 nm with an aspect ratio of 5.2, denoted by cyan arrows) and small particles (8.5 ± 2.5 nm, denoted by red arrows) formed a hybrid microstructure near the scratch surface (~150 nm below, PSS: ~2.0). Those Cr lamellae consisted of several nanograins (Fig. 7(c, d)) are composed of pure Cr according to TEM-EDS results (Fig. 7(b)). Cr lamellae were also detected in the locations below ~1 μm (Fig. 7(e)) and ~400 nm (Fig. 8(a)). These lamellae are single crystals (Fig. 7(e–g)). We note that such single-crystal Cr lamellae are also observed at a depth of 5.1 μm (Fig. 7(h)). Another important difference between the Cr lamellae at different depths is their aspect ratio. Cr lamellae in the sub-surface have a larger aspect ratio (~17 in Fig. 7(i)), while those close to the scratch surface have an aspect ratio closer to 5 (Fig. 7(a)). The observed variation in Cr lamellae aspect ratio as a function of depth is further illustrated in Fig. 7(h). The distinct characteristics in Cr lamellae in the top-most layer and the sub-surface reveal the important role of shear strain in the evolution of Cr dendritic grains surrounded by the Cu phase. At low shear strain in the sub-surface region, those Cr grains are dominated by equiaxed grains (Figs. 4(a) and 5(e)). As shear strain gradually increases towards the surface, the Cr lamellae form (Fig. 4(c)) and are further deformed to form sub-grains inside, giving rise to the polycrystalline lamellae at the top-most layer (Fig. 7(a–d), also see Fig. S3(d)). At the same time, some sub-grains are further detached from the parent lamellae due to the severe shear deformation, i.e., breakage of Cr lamellae (Figs. 7(a) and S7(c)). Therefore, Cr lamellae become closer to equiaxed progressively as shear strain increases. Our observation of hard Cr lamellae and particles in the soft Cu matrix is similar to the report of periodic harder Cu vortices formed in Ag/Cu and Al/Cu metallic multilayers during ultra-high shear strains [8]. The shared observation is that the harder phase always evolves into small particles in the soft matrix prior to the further inter-mixing at an even smaller scale.

To further delineate the formation process of Cr lamellae under high shear strain, we take a closer look at and propose an observation-based microscopic mechanism that involves effective shear slips and a debonding process. Fig. 8(a) shows a parent Cr lamella in the top surface layer (~400 nm below), where parallel low-angle grain boundaries (LAGBs) with lattice misorientation of ~6.5° are found (Fig. 8(a–d)). This special microstructure is likely the prerequisite configuration for the formation of Cr lamella. Given the proximity to the [110] zone of the Cr grain along the view direction (low tilting angles during TEM observation, $\alpha = 1.81°$ and $\beta = 2.97°$ in Fig. 8(b–d)) and the crystalline orientation of the lamella (FFT in Fig. 8(d)), it can be inferred that the applied shear stress (i.e., maximum resolved shear stress [MRSS] ~1) is parallel to the [110] zone axis on $(\bar{1}12)$ plane. Additionally, considering that both ends of a LAGBs terminate in the parent Cr grain (denoted by two red arrows in Fig. 8(b)), a relative slip of Cr at different depths along the SD direction (denoted by cyan arrows in Fig. S4(a)), and formation of single-crystal lamellae in a big parent Cr lamella (Figs. 7 and 8(a)), the LAGBs are presumed to be associated with shear slip along the SD direction (closed to [110]) on $(1\bar{1}2)$ planes (Fig. 8(c) and (e)). This shear is mainly associated with the MRSS plane and gradient shear strain from the top scratch surface to the bottom, although $(1\bar{1}2)$ is also one of the general slip planes ({110}, {112}, and {123}) in BCC crystals at room temperature [43]. Notably, the slips on $(\bar{1}12)$ (Fig. 8(e)) cannot be induced by a single $\frac{1}{2}\langle 111\rangle\{112\}$ screw dislocation [44], because the only slip direction ($[\bar{1}11]$) on $(\bar{1}12)$ is perpendicular to the [110] direction of MRSS. Nevertheless, these slips can be realized by the interactive slip-on planes experiencing the same or similar RSS along the $[11\bar{1}]$ and [111] slip directions (the resultant vector direction is [110]). Accordingly, the slip planes can be (112), (101), (011) and $(\bar{1}01)$, $(\bar{1}\bar{1}2)$, $(0\bar{1}1)$, respectively. Wherein, the screw dislocations $\frac{1}{2}[11\bar{1}](011)$ (RSS: ~0.82) and $\frac{1}{2}[111](\bar{1}01)$ (RSS: ~0.82) are the most possible group resulting in the formation of the slips on $(1\bar{1}2)$ planes along [110], similar to the reported {110} slip with {112} slip traces in BCC tungsten [45]. Around the tip region of the upper LAGBs segment (yellow box in Fig. 8(e)), a nearby screw dislocation is identified by the local strain contrast without net lattice mismatch (zero projected Burgers vector) in Fig. 8(f). The Burgers vector nature of this screw dislocation could be presumed to be $1/2\langle 111\rangle\{110\}$ [44, 46]. In addition, HR-TEM images (Fig. 8(e–g)) reveal there also are edge dislocations with extra half-planes on $(\bar{1}10)$ (such as the edge dislocation $\frac{1}{2}[\bar{1}11](101)$) and (002) (such as the edge dislocation $\frac{1}{2}[11\bar{1}](011)$) around the slip trace induced by RSS. The tilt angle (7.2°, Fig. 8(g)) induced by the edge dislocation on (002) is consistent with the measured tilt angles of the LAGBs (~6.5°, Fig. 8(c, d)). These edge dislocations can weaken the bond strength of the slip interfaces. Furthermore, with increasing cumulative shear deformation, i.e., continuous advancing of the shear slip and relative tilt of the Cr lamellae, the resolved shear stress perpendicular to the original [110] zone axis could be increased correspondingly and hypothetically translated to the incremental debonding of the slip interface. Then Cu can shear into the Cr block along the LAGBs (Fig. 8(a)), resulting in the splitting of the Cr lamellae from the block Cr grain (Figs. 8(h) and S5).

Considering the local shear geometry and the crystallography of the Cr grain around the LAGB tip, the formation of Cr lamella is schematized in Fig. 8(i). The entire evolution of Cr lamella in the top-most layer can be summarized as follows. First, Cr lamella is formed by shear slip and grain tilt induced debonding process. Then, the lamella is split from the Cr block due to the continuous shear deformation. Concurrently, the surrounding softer Cu phase is plasticized and flows into the space between the Cr lamellae. Finally, further fragmentation of the parent Cr lamella and formation of finer Cr particles is seen under the high shear strain.

3.5. Localized supersaturation of Cu nanoparticles and Cr nanograins

Supersaturation is significantly affected by grain refinement [19, 20], interface relationship [15], the difference in hardness [37], and

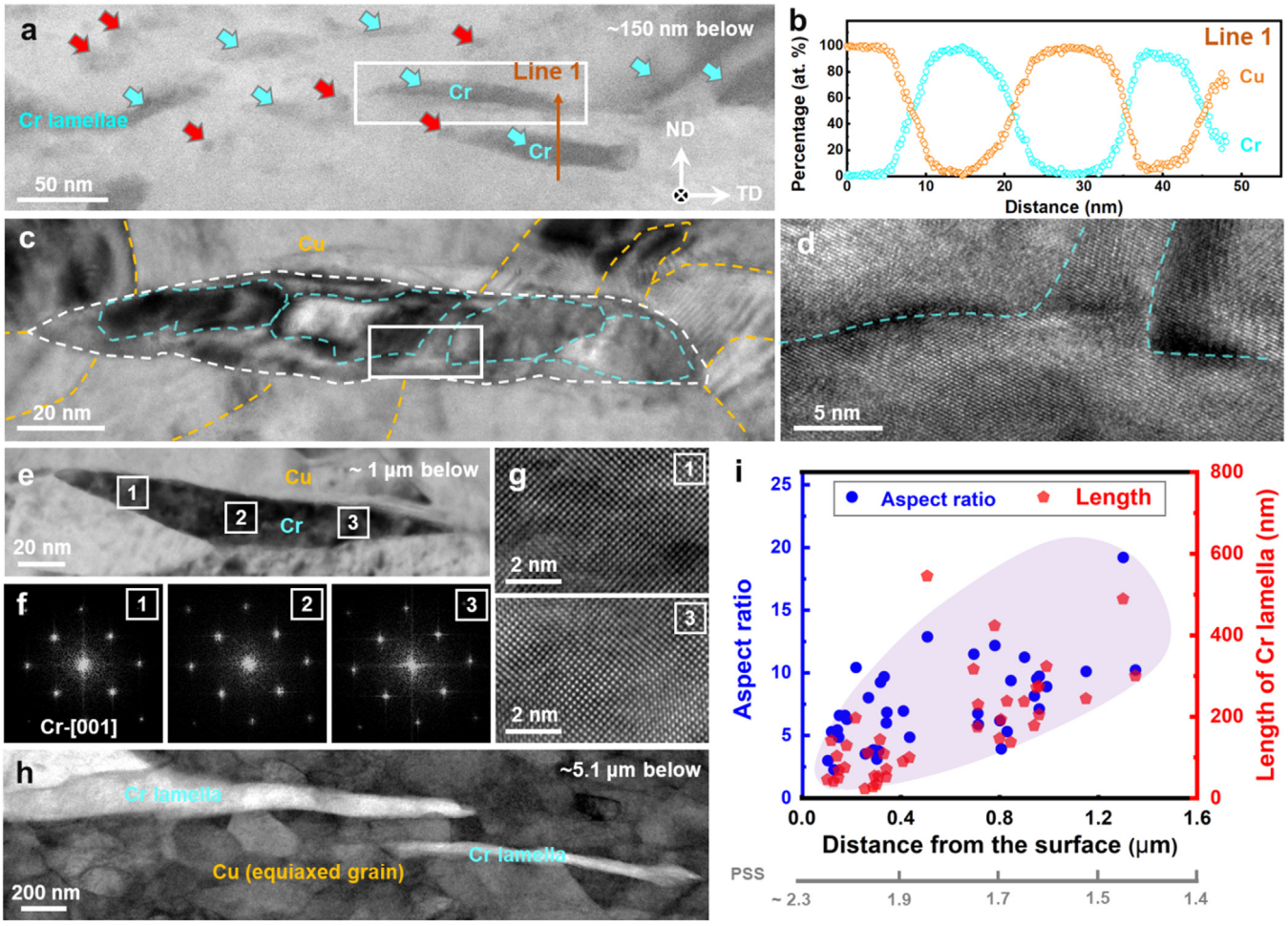

Fig. 7. Evolution of Cr lamellae in the Cu matrix after 10 cycles of severe shear deformation. (a) HAADF-STEM image showing the formation of many separated Cr lamellae (denoted by cyan arrows) and particles (denoted by red arrows) in the top surface of the Cu matrix. (b) EDS line scan along line 1 in (a). (c) BF-TEM image of the enlarged white box in (a) showing grain refinement of the Cr lamella. GBs in the Cr lamella and the surrounding Cu matrix are roughly outlined by cyan and orange dashed lines, respectively. The Cu/Cr interface is outlined by a white dashed line. (d) HR-TEM image of the white-boxed area in (c). (e) BF-TEM image of a Cr lamella. (f) FFT images of different locations in (e) verify that the Cr lamella is a single crystal. (g) HR-TEM images of locations 1 and 3 in (e) further verify the formation of the single-crystal Cr lamella. (h) ABF-TEM image showing the formation of two single-crystal Cr lamellae in the Cu matrix. (i) Variation of aspect ratio and length of the Cr lamella with the distance below the scratch surface.

other factors. Indeed, the dissolution tendencies of Cu NPs in Cr (Fig. 9(a–d)) and those of the Cr nanograins in Cu were observed to be remarkably different (Fig. 9(e–l)). As presented in Fig. 9(a–c), there is relative solute enrichment of Cr in the Cu NPs (~20 at.% Cr in the Cu particles). This forced mixing is induced by dislocations shearing from Cu/Cr coherent/semi-coherent interfaces, i.e., dislocation transfer induced mixing processes [15,16]. Iso-concentration surfaces of the Cu NPs (Fig. 9(d)) show that the selected area for composition analysis (Fig. 9(b, c)) is almost perpendicular to the front edge of the Cu NP. This corroborates the assertion that the concentration variation in the tip area of the Cu particle (Fig. 9(c)) comes from the mixing, rather than the projection of the inclined interface. Supersaturation was also detected around Cr nanograins based on APT analysis of seven nanoparticles in the top surface (Fig. 9(e–l)). But observations for Cr nanograins vary from particle to particle (Fig. 9(j–l), see also Fig. S9) and the highest concentration of Cu in Cr nanograins is ~10 at.% (Fig. 9(l)), relatively lower than that of Cr in Cu nanoparticles (~20 at.%, Fig. 9(c)) with a similar thickness (~4 nm), i.e., the mixing kinetics appeared to be asymmetric. In addition, supersaturation (if considering that the average Cu concentration in Cr is higher than 5 at.%) was detected in three out of the seven Cr nanograins in Cu in the top-surface (Figs. 9(e–l) and S9). Meanwhile, oxidation of Cr nanograins was also detected in the top surface, especially at the upper half of the particles (Fig. 9(f, g)). This means that Cr nanograins (particles 3–6, Fig. 9(e–g)) react with ambient oxygen during deformation preferentially. Notably, nanoparticles 3 and 5 were not employed for the line profile composition analysis, due to their severe oxidation.

3.5.1. *Effect of grain refinement*

Generally, grain refinement is considered a key step for subsequent forced chemical mixing [16]. As discussed above, DRX prevails Cu preferentially due to the strain localization (Figs. 4–6). DRX facilitates grain refinement of Cu, especially within Cu NPs in Cr observed in the initial microstructure (Figs. 4(d) and S4(f)). This is further verified by the formation of nano-domains in an initial Cu NP after severe shear deformation at the sub-surface (~2.9 μm, PPS: ~0.9, Fig. 10). The formation of the Cu nano-domains (Fig. 10) results from the dislocation shuffling process [9]. Notably, Cu NPs with a "diffuse" Cr/Cu interface contrast were detected in the topmost surface, especially in the area near the scratch surface (< 1 μm, PSS > ~1.6, Fig. S8(a, b)), indicating these Cu NPs were further sheared into the surrounding Cr grains compared with the Cu NPs in the sub-surface. In addition, no voids can be detected around these Cu nano-domains. Nevertheless, only a few Cr nanograins (length < 100 nm) were detected in the top-most

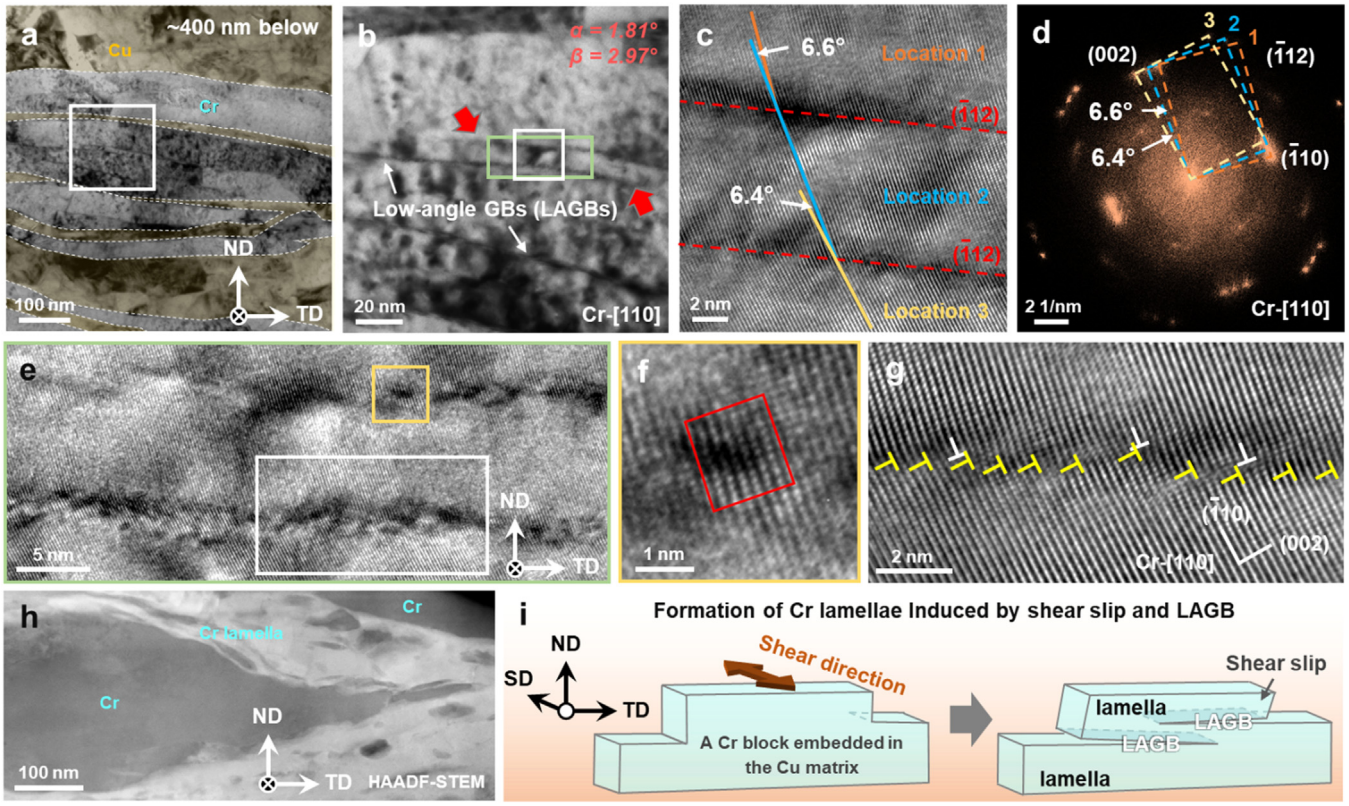

Fig. 8. Formation of Cr lamellae in the Cu matrix after 10 cycles of severe shear deformation. (a) BF-TEM image showing the formation of Cr lamellae in the Cu matrix in the ND–TD sample. The image was acquired from ~400 nm below the scratch surface. (b) Enlarged white boxed area in (a) showing formation of LAGBs in a Cr grain. (c) HR-TEM image of the white-boxed area in (b) showing lattice rotation on both sides of the LAGBs. α and β are tilt angles of the TEM holder. (d) FFT image of (c). (e) HR-TEM image of the green-boxed area in (b). (f) Enlarged yellow-boxed area in (e). (g) Enlarged white-boxed area in (e) showing profuse dislocations along the LAGB. Dislocations are denoted by "⊥". (h) HAADF-STEM image showing the formation of many Cr lamellae at the top-surface (~100 nm below) of a Cr block. (i) Schematic illustration showing the formation process of Cr lamellae in the Cu matrix.

layer (Figs. 7(a) and S7), which is very close to the scratch surface (Figs. 7(a) and S7(c)). Therefore, a relatively larger Cr grain size compared with that of Cu NPs embedded in Cr after similar deformation delays the mixing process.

3.5.2. Effect of interfacial relationship

Interfacial relationships of the nanoparticles with the surrounding grains are also crucial for mixing. Similar to the observed ORs between the Cu NPs and the surrounding Cr before deformation (Fig. 3), the deformed Cu NPs maintained an excellent N–W relationship with the surrounding Cr, although numerous Cu nano-domains formed after severe shear deformation at the subsurface (~2.9 μm, PPS ~0.9, Fig. 10). This verifies that the N–W OR presents excellent stability during deformation [47]. Besides Cu NPs in Cr, some Cu NPs were also detected at GBs after deformation. Nevertheless, the surrounding Cr grains are dominated by low-angle GBs (Fig. 5(e)). The interfacial relationships facilitate strain/dislocation transfer from Cr to Cu, i.e., massive dislocations can shear into Cu from the coherent/semi-coherent interfaces, inducing forced mixing. On the contrary, Cr nanograins are incoherent with the surrounding Cu grains (Fig. 7(c, d)), which are refined by DRX. Consequently, it is difficult for dislocations to transfer from Cu to Cr through the incoherent Cu/Cr interfaces [48], resulting in insignificant mixing in Cr nanograins. The formation of voids along the Cu/Cr interfaces in the top-most layer (Fig. S6) is supposed to be partially associated with a pile-up of dislocations and aggregation of numerous vacancies at the incoherent Cu/Cr interfaces during severe deformation.

3.5.3. Effect of mechanical incompatibility

The mechanical incompatibility between Cu and Cr also significantly affects the mass transport at the phase interface. In principle, the smaller the hardness difference between the two phases, the less strain localization in the softer phase facilitates forced mixing [37]. After deformation, the grain size of Cr is about two times of that Cu at similar depths (Figs. 4(d) and S4(f)), i.e., the Cu grains were refined more in comparison with that of Cr grains under similar deformation conditions. Nevertheless, the Hall–Petch coefficient of Cr (1380–2561 MPa $\mu m^{0.5}$ [49–51]) is significantly larger than that of Cu (316 MPa $\mu m^{0.5}$ [52]). This means that the grain refinement will result in further hardness disparity between Cu and Cr (Fig. S10). Therefore, the initial small Cu NPs (a small grain size: 54.2 ± 37.4 nm, the estimated hardness is ~4 GPa, Fig. S10) surrounded by Cr (a large dendritic crystal size: 11.8 ± 6.1 μm, the hardness is ~7.2 GPa) is the optimal condition for forced mixing in the experiment according to Hall–Petch relationship related to hardness evolution between Cu and Cr.

3.5.4. Effect of selective oxidization

Given the complex crystal structure of oxides and hardness difference between the oxides and the Cr nanoparticles, we propose that the oxide skin layer formed around Cr nanoparticles prevents further mass transport by suppressing movement of dislocations in the surrounding Cu matrix. Severe oxidation of small Cr particles (Fig. 9(f, g)) also remarkably reduces alloying process dominated by increasing the interfacial free energy of small particles [20], such as observed at the tip regions of the Cu NPs (Fig. 9(a–c)).

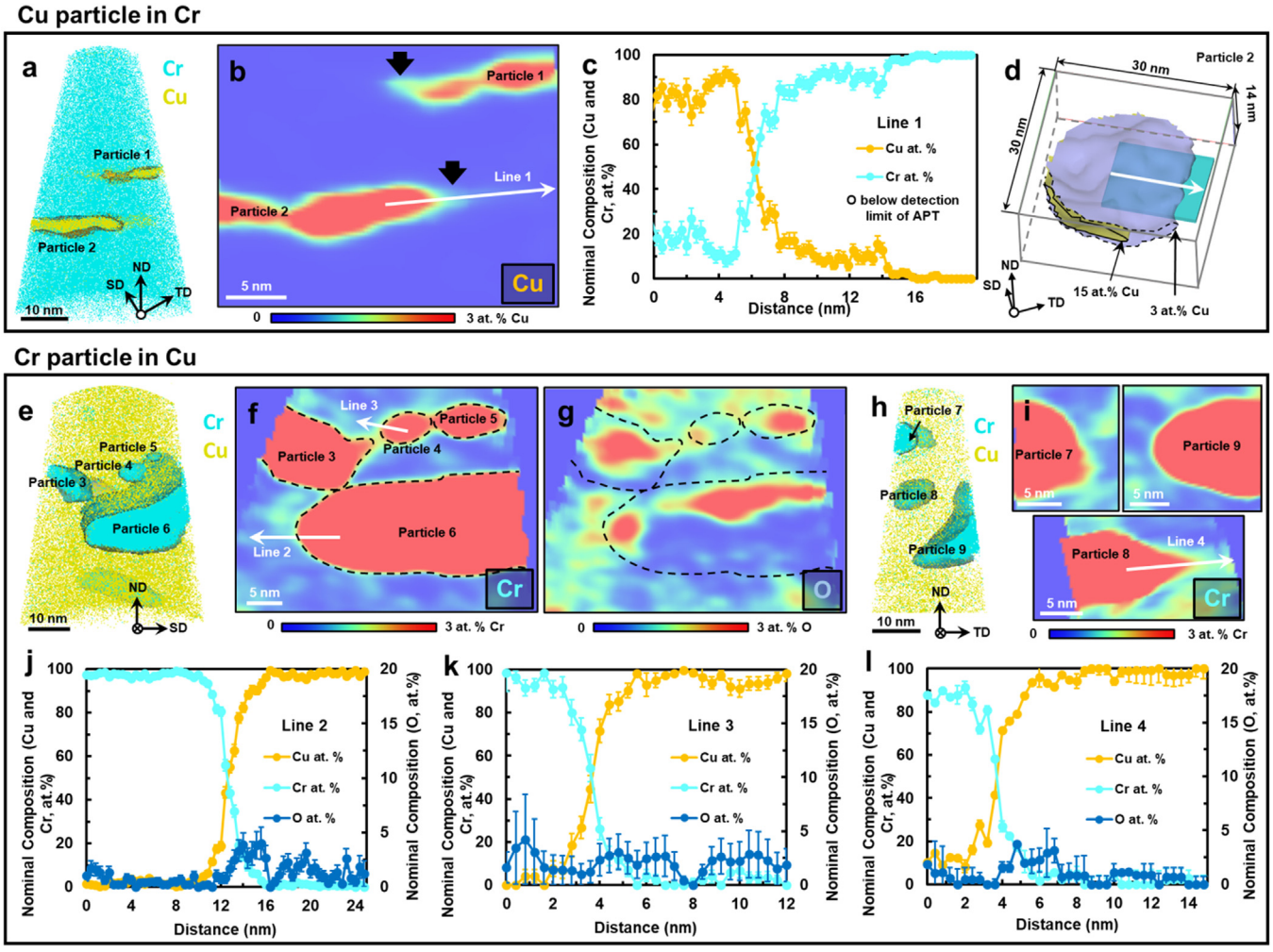

Fig. 9. Alloying analysis by atom probe tomography (APT) after 10 cycles of shear deformation. (a) APT reconstruction of two Cu NPs in the Cr. (b) 2-D contour plot highlighting the Cu concentration variation from a 2 nm (top) and 10 nm (bottom) slice. (c) Compositional change along the white arrow in (b). (d) 3-D isoconcentration surfaces of the Cu NP 2 in (a). 3 at.% (purple) and 15 at.% (yellow) Cu isoconcentration surfaces are displayed here to delineate the boundaries between Cu and Cr. (e, h) APT reconstruction of Cr nanograins in Cu. (f, i) 2-D contour plot highlighting the Cr concentration variation of Cr nanograins in (e) and (h), respectively. (g) 2-D contour plot highlighting the O concentration variation. (j–l) Compositional change along with white arrows 2–4, respectively. Notably, (a), (e), and (h) come from 50 nm, ~120 nm, and ~50 nm below the scratch surface, respectively.

3.5.5. Ab initio simulation of selective oxidation

To investigate the origin of the Cr oxidation at the incoherent Cu/Cr interface and an apparent lack of oxygen at the coherent interface, we quantified the stability of interstitial oxygen impurity (O_i) at selected locations at Cu/Cr interfaces as well as in Cu bulk and Cr bulk. The O atom incorporation energy was calculated as $E_{Oi} = E_{CuCrO} - E_{CuCr} - E_{O2}/2$, where E_{CuCrO} and E_{CuCr} were the total energies of the Cu–Cr system with and without O, respectively, and E_{O2} was the energy of the gas-phase O_2 molecule. The modeled Cu–Cr systems mimicking the experimentally observed interfaces (Fig. 9) are shown in Fig. S11(a–c): the coherent interface was represented using a Cu/Cr slab with KS interfacial orientation relationship (model A); incoherent interfaces were modeled using a Cr cluster of ~70 atoms embedded into the bulk Cu (Model B) and by a similar size Cu cluster embedded into the bulk Cr (Model C).

We found that O_i is significantly more stable at the Cu/Cr interfaces than in the Cu or Cr bulk lattices (Fig. 11(a)). Since the KS Cu/Cr interface is ordered, the O_i incorporation energy is the same for all interfacial sites. In contrast, incoherent interfaces (Model B and C) feature variability of the local structural environments, resulting in a spread of the O_i incorporation energies. We analyzed the O–*M* distances and *M*–O–*M* (*M*=Cu, Cr) angles (see Model Cu–Cr systems in Supplementary Information) and found that Cr atoms form an ordered incomplete octahedral environment for O_i, while the most stable O_i configurations correspond to larger O–Cu distances. Further from the incoherent interfaces, e.g., inside the Cr inclusion in Model B and inside the Cu inclusion in Model C, the O_i is also significantly more stable than in the ideal bulk (by 1.07 eV and 1.15 eV, respectively), pointing to the stabilizing role of the lattice distortions that can take place at these interfaces. We attribute these distortions to the excess volume (78 Å^3 and 159 Å^3 for models B and C, respectively) associated with incoherent interfaces. Furthermore, we note that volume per Cr in α-Cr_2O_3 (V_{Cr2O3}/n_{Cr}) is about twice that in Cr metal (V_{Cr}/n_{Cr}). Hence, excess volume is critical to accommodate the lattice expansion due to Cr oxidation. According to our estimates (see Model Cu–Cr systems in Supplementary Information), there is approximately 3 times more excess volume associated with our models of incoherent interfaces.

Finally, analysis of the electron charge distribution at the Cu/Cr interfaces (Fig. 11(b)) points to the charge disproportionation between Cr and Cu, which become positive and negative, respectively. The charge disproportionation is significantly larger for the incoherent interfaces (Fig. 11(b)) than for the coherent ones. In the presence of O_i at the Cu/Cr interface (Fig. 11(c)), Cu tends to re-

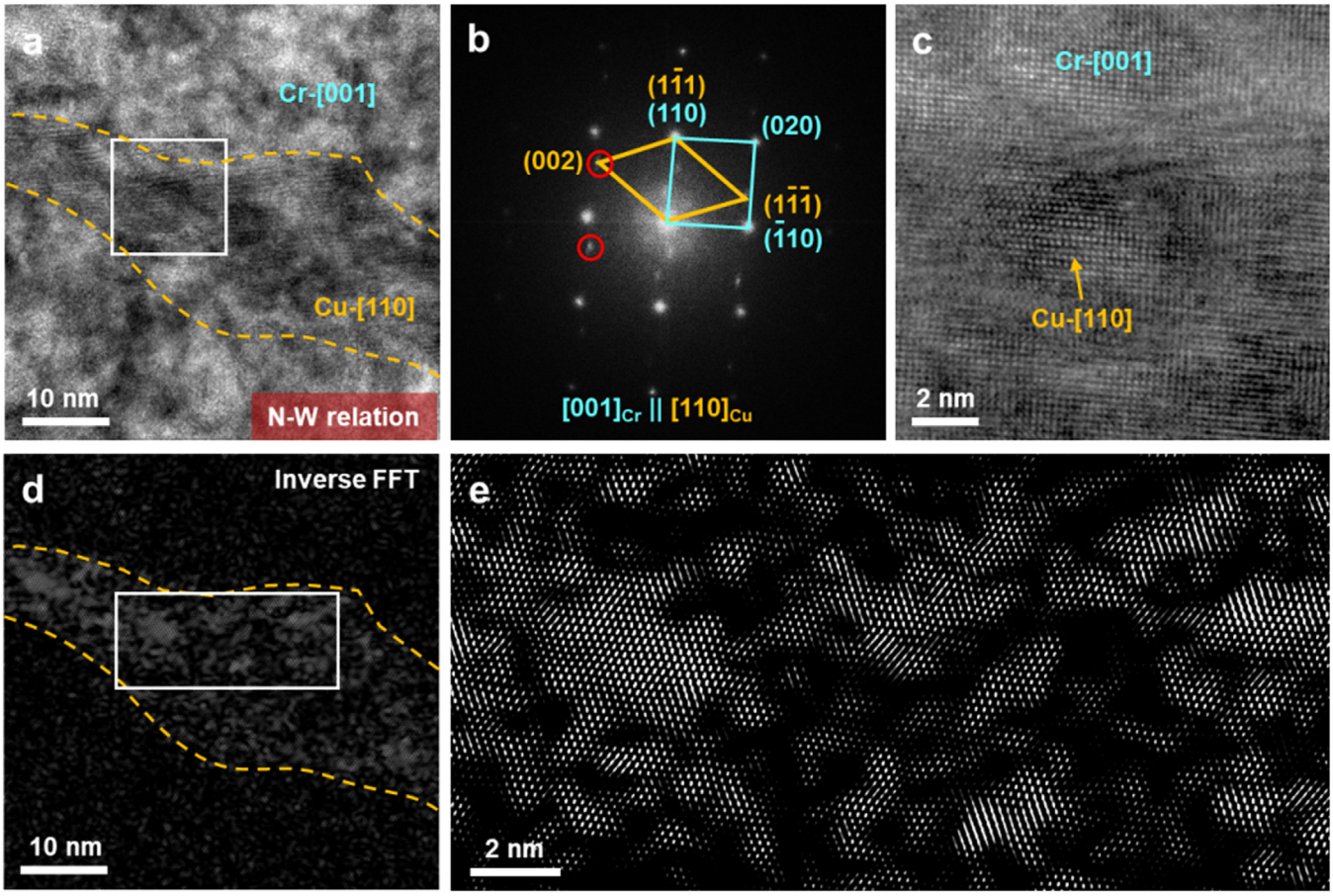

Fig. 10. Refinement of Cu NPs in the Cr matrix after 10 cycles of severe shear deformation. (a) HR-TEM image of a Cu particle in the Cr matrix (~2.9 μm below the scratch surface). The Cu/Cr interface is roughly outlined by yellow dashed lines. (b) FFT image of (a) showing the Cu particle maintains the N–W relation with the surrounding Cu matrix. (c) Enlarged white-boxed area in (a) showing the formation of a Cu domain in the original Cu NP. (d) Inverse FFT image of the selected diffraction spots [denoted by red circles in (b)] showing the formation of many Cu domains in the original Cu particle. (e) Enlarged white-boxed area in (d).

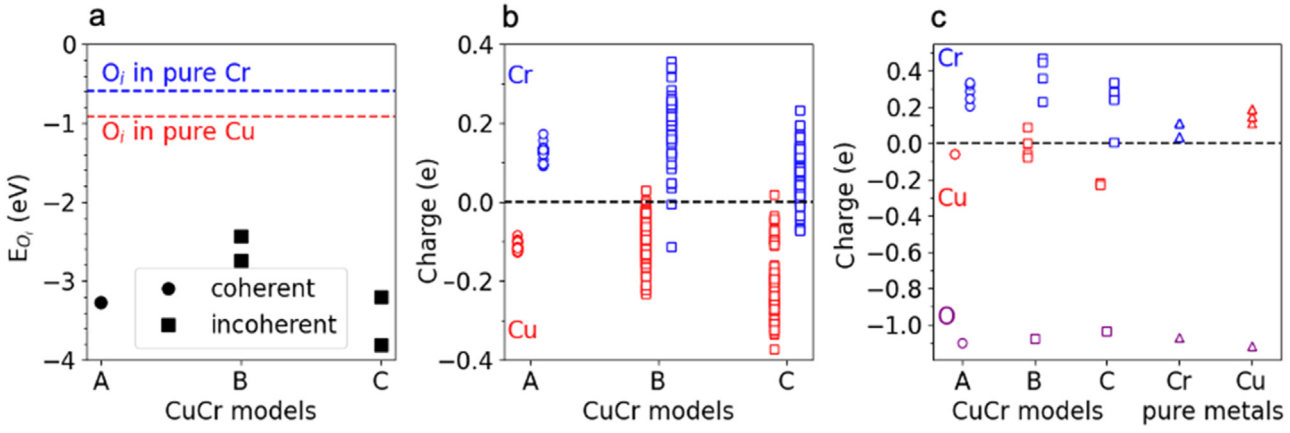

Fig. 11. Oxidization of various Cu/Cr interfaces simulated by Ab initio method. (a) Stability of interstitial O (O_i) at the coherent (Model A) and incoherent (Model B, C) Cu/Cr interfaces (see also Fig. S11) and in the pure bulk Cu and Cr. (b, c) Atomic charge distribution at the Cu/Cr interfaces (b) and in the presence of O_i (within 3 Å from O_i) (c). The configurations of Model B and C chosen to show charge distribution in panel c are the ones with lower energy in panel a.

tain its negative charge, while Cr becomes even more positively charged, consistent with the prevalence of ionic Cr–O bonds.

To summarize, the larger charge disproportionation and higher excess volume at the incoherence interfaces allow for the formation of stronger ionic Cr–O bonds, relaxation of the lattice upon trapping O_i and a larger amount of trapped oxygen. While KS interfaces also can trap O_i, the lack of free volume needed for the lattice relaxation for oxide layer growth suppresses O_i accumulation there. These conclusions are consistent with the experimental observations of the oxygen distribution in the vicinity of incoherent interfaces (Fig. 9).

4. Conclusions

Here, a high mixing enthalpy binary alloy (Cu–50 at.% Cr) was employed as a model system to investigate microstructure evolu-

tion, mass transport, and SSS tendencies due to forced mixing between Cu and Cr phases after severe shear deformation. The major results are summarized as follows:

(1) During severe shear deformation, grain refinement was detected in both Cu and Cr grains as a function of shear strain. However, the grain sizes of Cu are smaller than those of Cr after undergoing a similar extent of deformation, due to preferential DRX of Cu.
(2) Cu NPs embedded in Cr maintain excellent coherent relationships with the surrounding Cr grains after deformation, even though the microstructure of Cu NPs was modified significantly, by the formation of nano-domains (~2–5 nm). Cr nanograins were mainly detected in the top-most layer (< ~200 nm below the scratch surface).
(3) Cr nanograins are formed by refinement of Cr lamellae, which are split from block Cr grains by plastically flowing Cu after the bond strength between lamellae is weakened significantly by continuous shear slip and grain tilt during severe shear deformation.
(4) A distinct supersaturation difference between the Cu NPs (evolved by the initial Cu NPs embedded in Cr) and Cr nanograins (surrounded by Cu and formed by continuous grain refinement) was detected by APT analysis. A relatively higher level of supersaturation was found in the Cu NPs than in the Cr nanograins, due to preferential DRX of Cu, excellent Cu NPs/Cr orientation relationships, and relative small hardness difference between the initial Cu NPs and the surrounding Cr grains.
(5) Incoherency of Cr with the surrounding Cu grains impedes dislocations transmission from Cu to Cr and results in the formation of voids at the Cu/Cr interfaces and relative low mixing in the Cr nanoparticles.
(6) Oxidation of Cr was detected in the top surface, especially for the tiny nanoparticles, the tip areas of the Cr nanograins, and the upper half of the Cr nanograins. Ab initio simulation verifies that Cr presents a higher tendency to be oxidized by O than Cu at the incoherent Cu/Cr interfaces. The formation of oxide may prevent the further dissolution of Cr nanograins as well.

These findings suggest that the coherent Cu NPs in the Cr grains facilitate forced mixing during shear deformation, providing a better understanding of the coupling between severe shear deformation and mass transport in the immiscible Cu–50 at.% Cr alloy.

Acknowledgments

This research was supported by the Laboratory Directed Research and Development (LDRD) Solid Phase Processing Science Initiative (SPPSi), at the Pacific Northwest National Laboratory (PNNL). Partial TEM experiments of this work were conducted in the William R. Wiley Environmental Molecular Sciences Laboratory (EMSL), a national scientific user facility sponsored by the DOE Office of Biological and Environmental Research and located at PNNL. The ab initio calculations were performed using PNNL Institutional Computing (PIC) service. PNNL is a multiprogram national laboratory operated by Battelle Memorial Institute for the U.S. Department of Energy (DOE) under contract No. DE-AC05–76RL01830.

Supplementary materials

Supplementary material associated with this article can be found, in the online version, at doi:10.1016/j.jmst.2022.06.029.

References

[1] H.J. Fecht, E. Hellstern, Z. Fu, W.L. Johnson, Metall. Trans. A 21 (1990) 2333–2337.
[2] V.M. Segal, Mater. Sci. Eng. A 271 (1999) 322–333.
[3] M. Zelin, Acta Mater. 50 (2002) 4431–4447.
[4] A.P. Zhilyaev, T.G. Langdon, Prog. Mater. Sci. 53 (2008) 893–979.
[5] Z.Y. Ma, Metall. Mater. Trans. A 39 (2008) 642–658.
[6] B. Gwalani, M. Olszta, S. Varma, L. Li, A. Soulami, E. Kautz, S. Pathak, A. Rohatgi, P.V. Sushko, S. Mathaudhu, C.A. Powell, A. Devaraj, Commun. Mater. 1 (2020) 85.
[7] E. Ma, Prog. Mater. Sci. 50 (2005) 413–509.
[8] M. Pouryazdan, B.J.P. Kaus, A. Rack, A. Ershov, H. Hahn, Nat. Commun. 8 (2017) 1611.
[9] D. Raabe, S. Ohsaki, K. Hono, Acta Mater. 57 (2009) 5254–5263.
[10] M. Wang, R.S. Averback, P. Bellon, S. Dillon, Acta Mater. 62 (2014) 276–285.
[11] S. Odunuga, Y. Li, P. Krasnochtchekov, P. Bellon, R.S. Averback, Phys. Rev. Lett. 95 (2005) 045901.
[12] E. Botcharova, J. Freudenberger, L. Schultz, J. Mater. Sci. 39 (2004) 5287–5290.
[13] E. Ma, J.H. He, P.J. Schilling, Phys. Rev. B 55 (1997) 5542–5545.
[14] J. Xu, U. Herr, T. Klassen, R.S. Averback, J. Appl. Phys. 79 (1996) 3935–3945.
[15] Y. Ashkenazy, N.Q. Vo, D. Schwen, R.S. Averback, P. Bellon, Acta Mater. 60 (2012) 984–993.
[16] E. Ma, H.W. Sheng, J.H. He, P.J. Schilling, Mater. Sci. Eng. A 286 (2000) 48–57.
[17] J. Eckert, J.C. Holzer, C.E. Krill, W.L. Johnson, J. Appl. Phys. 73 (1993) 2794–2802.
[18] T.D. Shen, K.Y. Wang, M.X. Quan, J.T. Wang, Mater. Sci. Forum 88-90 (1992) 391–398.
[19] A.R. Yavari, P.J. Desré, T. Benameur, Phys. Rev. Lett. 68 (1992) 2235–2238.
[20] X. Sauvage, P. Jessner, F. Vurpillot, R. Pippan, Scr. Mater. 58 (2008) 1125–1128.
[21] C.W. Sinclair, J.D. Embury, G.C. Weatherly, Mater. Sci. Eng. A 272 (1999) 90–98.
[22] Q. Mao, Y. Zhang, Y. Guo, Y. Zhao, Commun. Mater. 2 (2021) 46.
[23] X. Yang, D. Shen, H. Zhang, W. Tong, Vacuum 146 (2017) 225–232.
[24] A. Chbihi, X. Sauvage, D. Blavette, Acta Mater. 60 (2012) 4575–4585.
[25] J.H. Dautzenberg, J.H. Zaat, Wear 23 (1973) 9–19.
[26] G. Kresse, J. Furthmüller, Phys. Rev. B-Condens Matter 54 (1996) 11169–11186.
[27] G. Kresse, J. Hafner, Phys. Rev. B-Condens Matter 47 (1993) 558–561.
[28] P. Hohenberg, W. Kohn, Phys. Rev. 136 (1964) 864–871.
[29] J.P. Perdew, K. Burke, M. Ernzerhof, Phys. Rev. Lett. 77 (1996) 3865–3868.
[30] J.P. Perdew, K. Burke, M. Ernzerhof, Phys. Rev. Lett. 78 (1997) 1396.
[31] P.E. Blöchl, Phys. Rev. B 50 (1994) 17953–17979.
[32] G. Henkelman, A. Arnaldsson, H. Jónsson, Comput. Mater. Sci. 36 (2006) 354–360.
[33] S. Wang, S. Han, G. Xin, J. Lin, R. Wei, J. Lian, K. Sun, X. Zu, Q. Yu, Mater. Des. 139 (2018) 181–187.
[34] M.G. Hall, H.I. Aaronson, K.R. Kinsma, Surf. Sci. 31 (1972) 257–274.
[35] M.G. Hall, H.I. Aaronson, Acta Metall. 34 (1986) 1409–1418.
[36] T. Fujii, H. Nakazawa, M. Kato, U. Dahmen, Acta Mater. 48 (2000) 1033–1045.
[37] Z.C. Cordero, C.A. Schuh, Acta Mater. 82 (2015) 123–136.
[38] T. Sakai, A. Belyakov, R. Kaibyshev, H. Miura, J.J. Jonas, Prog. Mater. Sci. 60 (2014) 130–207.
[39] K. Huang, R.E. Logé, Mater. Des. 111 (2016) 548–574.
[40] J. Ribbe, D. Baither, G. Schmitz, S.V. Divinski, Phys. Rev. Lett. 102 (2009) 165501.
[41] K. Wang, N.R. Tao, G. Liu, J. Lu, K. Lu, Acta Mater. 54 (2006) 5281–5291.
[42] G. Yang, K. Du, D. Xu, H. Xie, W. Li, D. Liu, Y. Qi, H. Ye, Acta Mater. 152 (2018) 269–277.
[43] C.R. Weinberger, B.L. Boyce, C.C. Battaile, Int. Mater. Rev. 58 (2013) 296–314.
[44] M.R. Gilbert, S. Queyreau, J. Marian, Phys. Rev. B 84 (2011) 174103.
[45] C. Marichal, H. Van Swygenhoven, S. Van Petegem, C. Borca, Sci. Rep. 3 (2013) 2547.
[46] M. Yamaguchi, V. Vitek, J. Phys. F: Met. Phys. 3 (1973) 523–536.
[47] T.C. Kaspar, Q. Pang, P.V. Sushko, M.E. Bowden, J. Tao, B. Gwalani, M. Olszta, M. Efe, A. Devaraj, A. Rohatgi, Scr. Mater. 194 (2021) 113635.
[48] N.Q. Vo, J. Zhou, Y. Ashkenazy, D. Schwen, R.S. Averback, P. Bellon, JOM 65 (2013) 382–389.
[49] C.P. Brittain, R.W. Armstrong, G.C. Smith, Scr. Metall. 19 (1985) 89–91.
[50] V. Provenzano, R. Valiev, D.G. Rickerby, G. Valdre, Nanostruct. Mater. 12 (1999) 1103–1108.
[51] D. Wu, J. Zhang, J.C. Huang, H. Bei, T.G. Nieh, Scr. Mater. 68 (2013) 118–121.
[52] J. Chen, L. Lu, K. Lu, Scr. Mater. 54 (2006) 1913–1918.